J. metamorphic Geol., 2004, **22,** 475–494 doi:10.1111/j.1525-1314.2004.00527.x

Silica depleted melting of pelites. Petrogenetic grid and application to the Susqueda Aureole, Spain

M. RIESCO[1,2], K. STÜWE[1], J. RECHE[2] AND F. J. MARTINEZ[2]
[1]*Department of Geology and Palaeontology, University of Graz, Heinrichstrasse 26, A-8010 Graz, Austria (kurt.stuewe@uni-graz.at)*
[2]*Department of Geology, Universitat Autonoma de Barcelona, Edifici C Sur, 08193 Bellaterra, Spain*

ABSTRACT Metapelitic rocks in the low pressure contact metamorphic aureole around the Susqueda igneous complex, Spain show a number of features that make them an ideal testing ground for the modelling of silica-undersaturated melting. Rocks in the aureole experienced localized depletion in silica by the segregation of quartz veins during a pre-anatectic, regional cordierite-andalusite grade metamorphic event. These rocks were then intruded by gabbroic to dioritic rocks of the Susqueda igneous complex that formed a migmatitic contact metamorphic aureole in the country rocks. This migmatisation event caused quartz-saturated hornfels and restite formation in rocks that had experienced no quartz vein segregation in the previous regional metamorphic event, but silica-undersaturated melting in those rocks that were previously depleted in silica. Silica-undersaturated melting is investigated using a new petrogenetic *P–T* projection and equilibrium pseudosections calculated in the KFMASH and NCKFMASH systems, respectively. The grid considers quartz absent equilibria and a range of phases that form typically in silica-undersaturated bulk compositions, for example corundum. It is shown that the quartz-rich precursors in the Susqueda contact aureole produced about 10% melt during contact metamorphism. However, most of this melt was extracted leaving behind rocks with restitic bulk compositions and minor leucosome segregation. It is suggested that the melt mixed with the host igneous rocks causing an apparent magmatic zoning from diorite in the centre of the complex to tonalite at the margins. In contrast, the quartz-poor precursors (from which the quartz veins segregated) melted in the silica-undersaturated field producing a range of assemblages including peritectic corundum and spinel. Melting of the silica-undersaturated rocks produced only negligible melt and no subsequent melt loss.

Key words: corundum; melting; petrogenetic grid; silica depletion; Susqueda Spain.

INTRODUCTION

One of the most important steps in the rapid development of internally consistent thermodynamic data has been the incorporation of silicate melt into such data sets. As a consequence it is now possible to model the evolution of migmatites across the solidus in systems that approach real rock compositions (Holland & Powell, 1998; White *et al*., 2001). Several recent studies have used in these models to show that many migmatites – previously often thought to contain only *in situ* melts – must have been characterized by massive melt loss, even on a local scale (Powell & Downes, 1990; White & Powell, 2002; Johnson *et al*., 2003a). This is consistent with the observation that migmatites with pelitic precursors contain generally restitic parageneses that are rich in Fe–Mg phases (e.g. garnet and cordierite) but are depleted in silica and alkalis (Kriegsman, 2001).

Although such restite formation has usually been described with thermodynamic models that assume quartz in excess, many restite parageneses cannot be described with phase diagrams simplified by this assumption. For example, in pelitic precursors that were *not* rich in quartz, melting and melt loss may lead to a complete exhaustion of quartz and ultimately to the formation of silica-undersaturated parageneses including corundum (Grant, 1985; Cartwright & Barnicoat, 1986; Pattison & Harte, 1991). Similarly, restite parageneses including quartz are known to be extremely coarse-grained (up to 10 cm garnet-cordierite crystals; e.g. Stüwe & Powell, 1989a,b; White *et al*., 2003) so that it becomes questionable if quartz can still be considered to be part of the 'effective bulk composition' (Stüwe, 1997).

In this paper, a new petrogenetic grid for anatectic pelites is presented in the model system KFMASH in which quartz is not considered to be in excess. The model includes silicate phases common to migmatitic low-*P* high-*T* terranes and the grid is tested with thermodynamic pseudosections appropriate to bulk compositions of metapelitic precursors in the Susqueda contact aureole, Spain. The rocks from the Susqueda aureole provide an ideal testing ground as they include both quartz-rich and -poor pelitic precursors of otherwise very similar bulk composition.

THE PETROGENETIC GRID

The petrogenetic *P–T* projection for the model system KFMASH was calculated with the software THERMOCALC 3.1. (Powell & Holland, 1988) and the thermodynamic data set of Holland & Powell (1998), updated 19/09/99). The melting model, implementation of activity–composition relationships and all other model assumptions follow White *et al.* (2001). The present study differs from theirs in two aspects. First, and essential to this paper, quartz absent equilibria and some additional phases, e.g. corundum are considered. Secondly, Na_2O and CaO are initially not considered in the model system although they are important elements in metapelitic rocks. Phase relations of pelites in the NCKFMASH system are largely controlled by the phase relations in the subsystem KFMASH, which in turn is governed by the subsystem KASH. Therefore, most important aspects of the topology of the NCKFMASH projection can be shown in the more simple KFMASH system (Spear *et al.*, 1999; White *et al.*, 2001). This is because the addition of CaO and Na_2O introduces only one phase, plagioclase, and KFMASH univariant reactions become divariant fields in *P–T* space that are subparallel to their KFMASH univariant equivalents. Phase relationships are first presented in the system KASH and later expanded into the KFMASH system. The grid is then related to pseudosections in the NCKFMASH system and we use those to explain rocks from the Susqueda contact aureole.

KASH system

The calculated *P–T* projection in the system KASH for both silica-saturated and -undersaturated rocks is shown in Fig. 1. The phases considered are muscovite, aluminosilicate, K-feldspar, quartz, corundum, liquid (L) and H_2O, with the mineral abbreviations proposed by Kretz (1983). Calculated compatibility diagrams are shown for some of the relevant reaction spaces. Note that corundum, muscovite and K-feldspar are collinear in compositional space, causing the occurrence of several degenerate reactions related to muscovite breakdown. The compatibility diagrams are projected from H_2O although the assumption of water in excess is only realistic for extremely water-rich suprasolidus bulk compositions (Spear *et al.*, 1999). Within the considered *P–T* range, only two of a total of seven possible invariant points are stable. The invariant point [Crn] was already determined by other authors (White *et al.*, 2001). It fits qualitatively with the topology constrained by numerous experimental studies (e.g. Patiño Douce & Johnston, 1991; Holtz & Johannes, 1996). The quartz absent reaction was added to this point and found to be stable at high temperatures and crossing with equilibria that involve corundum at the invariant point [Qtz]. It connects two subparallel KASH univariant melting reactions that are important for the topology in KFMASH. One is a congruent quartz consuming reaction that forms the solidus and is located at about *c.* 700 °C at *c.* 5 kbar and *c.* 750 °C at *c.* 1 kbar: Sil + Kfs + Qtz + H_2O = L. The other is an incongruent quartz absent univariant reaction from *c.* 750 °C at *c.* 6.3 kbar to *c.* 850 °C at *c.* 1 kbar. The compatibility diagrams show that, in the KASH system, silica-poor bulk compositions (below the sillimanite–K-feldspar tie line; an example is indicated by an asterisk in Fig. 1) do not melt when crossing the congruent melting reaction Sil + Kfs + Qtz + H_2O = L. They first begin to melt at temperatures above the sillimanite–K-feldspar breakdown.

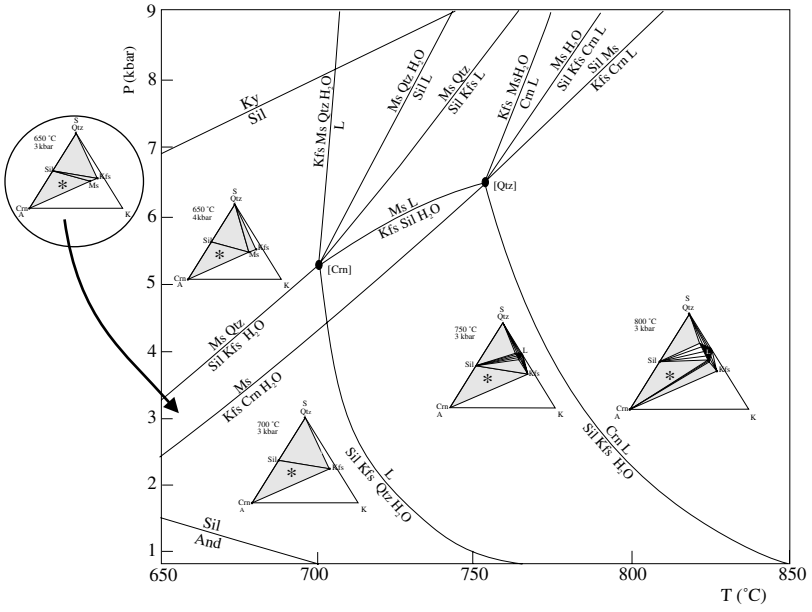

Fig. 1. Petrogenetic grid in the system KASH for both silica-saturated and quartz absent melting equilibria. Considered phases are muscovite, aluminosilicate, K-feldspar, quartz, corundum, liquid and H_2O. Compatibility diagrams are included in those fields with relevance in low-*P* aureoles. A = Al_2O_3, S = SiO_2 and K = $8K_2O$. The K_2O apex is enlarged as the projection of the K-bearing phases would be very close to the A–S line. Trivariant fields are shaded and the asterisk indicates a typical silica-poor bulk composition.

KFMASH system

The addition of FeO and MgO to the model adds significant complexity to the grid shown in Fig. 1, but is essential for the understanding of anatectic pelites. In addition to the phases considered in KASH, five more phases are now considered: garnet, biotite, cordierite, spinel and orthopyroxene. No phases are assumed to be in excess. The starting point for the construction of this grid was the topology derived from the KASH system and the KFMASH grid calculated in White *et al.* (2001). Although both the grid proposed here (Fig. 2) and that of White *et al.* (2001) are constructed with the same thermodynamic data set (Holland & Powell, 1998) there are slight differences in those invariant points involving spinel. This is because a simple ideal mixing model for spinel was used here. Thus, differences in the four invariant points were found in a narrow area around 3 kbar (Fig. 2b).

The general topology of the KFMASH grid is controlled by the subsystem KASH with the occurrence of two melting reactions that emanate from the quartz bearing and quartz absent invariant points between 3 and 4 kbar towards lower pressures. Many KFMASH reactions below 3 kbar terminate in KFASH invariant points towards lower pressure. This indicates that these reactions will only be seen by extremely iron rich bulk compositions and are unlikely to be of relevance to most pelitic bulk compositions. Correspondingly, the corundum producing reaction Crd + Mu = Bt + Kfs + Sil + Crn + H_2O (which appears on the left margin of Fig. 2 around 2.5 kbar and which relates to the KASH reaction Mu = Kfs + Crn + H_2O in Fig. 1) terminates in a KMASH invariant point so that it will only be seen by extremely magnesian bulk compositions. Nevertheless, several univariant reactions in Fig. 2 continue to very low pressures in the full KFMASH system, for example the quartz absent reaction Sil + Bt = Crd + Spl + Kfs + Crn + H_2O (labelled with a white arrow in Fig. 2). This reaction is responsible for the formation of corundum and spinel and has been recognized in other terranes, for example in the Ballachuslish low-*P* aureole (Pattison & Harte, 1991). The stability of several other reactions is also qualitatively consistent with other studies. For example, the reaction Sil + Bt + Qtz = Grt + Crd + Kfs + L is consistent with experimental calibrations of Carrington & Harley (1995) (labelled with black arrow in Fig. 2). Correspondingly, the stabilities of several quartz absent reactions are qualitatively in concordance with results obtained by McDade & Harley (2001); for example, the reaction Grt + Sil + Bt = Crd + Spl + Kfs + L is stable in the *P–T* window shown here (grey arrow).

A TESTING GROUND: THE SUSQUEDA AUREOLE

The new grid discussed above is useful for the interpretation of silica-undersaturated rocks. One example where there is a range of interesting parageneses related to silica-undersaturated melting at low pressures is the Susqueda contact aureole in Catalonia, Spain. There, metapelitic precursors experienced localized depletion in silica by the segregation of syn-D2 quartz veins during a pre-anatectic regional syn-D2 cordierite-andalusite grade metamorphic event (Reche & Martinez, 2002). These rocks were then intruded by the Susqueda igneous complex that formed a migmatitic contact metamorphic aureole in the rocks (Duran, 1985). This migmatisation event caused 'normal' restite formation in those rocks that had experienced no quartz vein segregation in the previous regional metamorphic event, but apparently silica-undersaturated melting in rocks that were previously depleted in quartz (see below). The contact aureole provides therefore an example of both silica-saturated and -undersaturated melting of the same precursor and metamorphic grade that can be compared.

Geological setting

The Susqueda complex (Fig. 3a) is a Variscan subconcordant intrusive complex that crops out over around 3 km^2 in the Guilleries Massif at the northeastern end of the Catalonian Coastal Ranges in Spain. The igneous rocks formed a contact metamorphic aureole that crosscuts a regional Variscan low-*P* metamorphic zonation. In the area of interest this regional metamorphic event is of cordierite-andalusite grade (Duran, 1985; Sebastian *et al.*, 1990; Reche & Martinez, 2002). However, in contrast to other contact metamorphic aureoles (Bowers *et al.*, 1990; Pattison & Harte, 1991) no contact metamorphic isograds can be mapped because the Susqueda aureole has a sill shape with multiple interfingerings with the host rocks in which contact effects are not evident further than 10 m away from any intrusive rock outcrop. For the purpose of this study, it is important to discern the following rock types (Fig. 3b): (1) *Micaschists*: These are the regional metamorphic cordierite-andalusite grade metapelites outside the contact aureole. They may or may not contain quartz veins. (2) *Hornfels-I*: These are pelitic hornfelses with evidence for partial melting in the outer part of the contact aureole. (3) *Hornfels-II*: This is a peculiar group of hornfelses containing spinel and/or corundum-bearing assemblages. These rocks are silica-undersaturated and occur as haloes around quartz veins (Fig. 4a,b). They are interpreted to have formed from the country rocks from which quartz veins were previously segregated. (4) *Restites:* These rocks occur in innermost part of the Susqueda igneous complex or as inclusions within it (Fig. 3b). (5) The intrusive rocks themselves consist of a wide range of calc alkaline rocks including ultramafic cumulates, gabbros, diorites and tonalites.

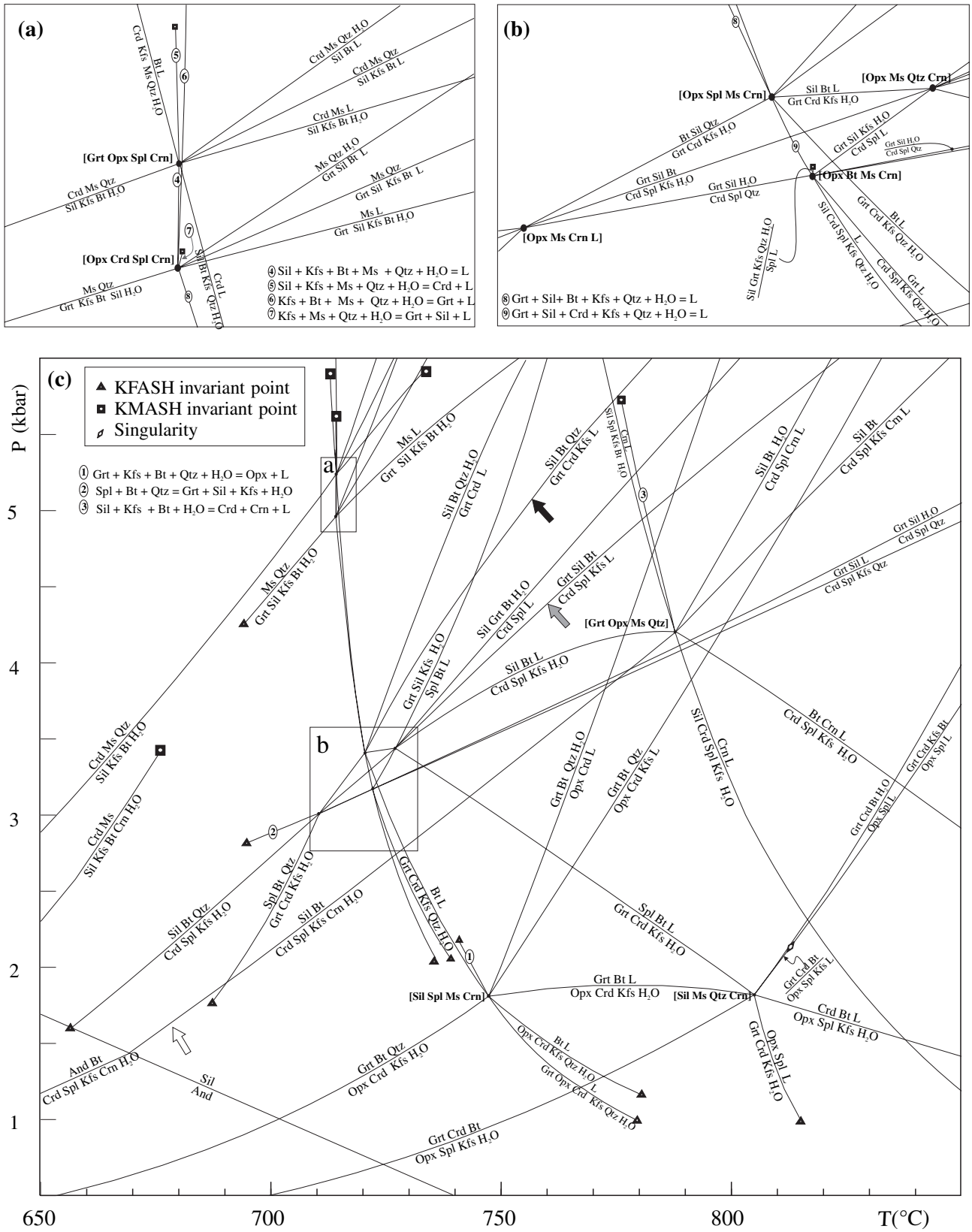

Fig. 2. Petrogentic grid for the system KFMASH for the phases: garnet, orthopyroxene, aluminosilicate, cordierite, spinel, biotite, K-feldspar, muscovite, quartz, corundum, liquid, and H_2O with no phases assumed in excess. See text for details.

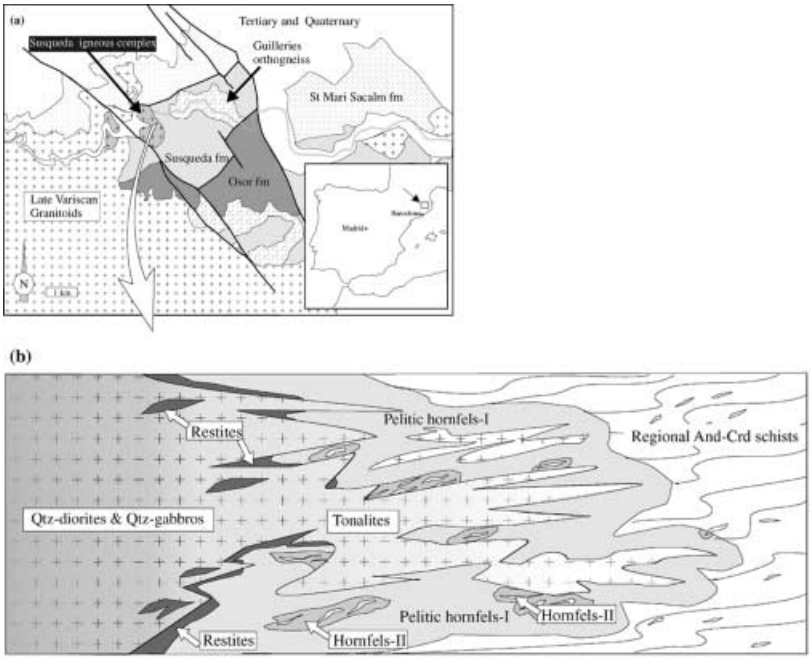

Fig. 3. (a) Geological map of the Guilleries massif; modified after Duran (1985). (b) Schematic profile and distribution of the different rock types in the Susqueda igneous aureole.

Petrography

This section presents the petrographic details of all rock types necessary for their interpretation on *P–T* pseudosections. Details of the mineral chemistry and analytical methods are summarised in the Appendix.

Micaschists

The regional metamorphic rocks exposed outside the contact aureole are well-equilibrated rocks with a porphyroblastic texture. Mica and elongated quartz define a composite Variscan fabric (S2) which is the main foliation in the region (Duran, 1985). Pelitic layers are interbedded with quartz-rich psamitic layers on a millimetre scale. Most pelitic layers contain the typical peak assemblage cordierite + andalusite + biotite + muscovite + quartz with or without staurolite porphyroblasts. Biotite and – in a lower proportion – muscovite are common minerals in both the psamitic and pelitic layers (Table 1). Andalusite occurs as subhedral porphyroblasts up to centimetres in size. They contain abundant inclusions of fine-grained quartz, mica and oxides. The inclusion trails may be spiral shaped suggesting a syn-tectonic growth of the porphyroblasts. Cordierite, where present, occurs as oval-shaped anhedral poikiloblasts up to 1 cm in size. Cordierite is often altered to pinite at the rims. Muscovite and biotite are aligned in the main schistosity, although fine-grained randomly oriented biotite has also been observed. Other minor minerals are Na-rich plagioclase, associated with quartz, and accessory ilmenite and occasionally secondary magnetite. Staurolite occurs in iron-rich schists forming porphyroblasts wrapped by the foliation and partially resorbed into andalusite-biotite aggregates. Biotite-rich pressure shadows are common.

An important feature of these rocks is the local segregation of quartz veins. These quartz veins occur typically in groups (Fig. 4a,b). They are usually lens-shaped and are up to 10 cm wide, usually less than a metre long and their orientation indicates that they formed during the pre-anatectic regional metamorphic and deformation event. While the processes associated with this early segregation and migration of silica in the micaschists is in itself an interesting process, it is not discussed further here, and the interested reader is referred to Reche & Martinez (2002) for further details. Here it is only important that these quartz veins are associated with silica-depleted haloes: close to the contact with these quartz veins (Fig. 3b) the schists show a special assemblage that lacks muscovite and the mode of quartz is dramatically reduced. These selvages are up to several decimetres wide and are characterized by a somewhat darker colour in the field (Fig. 4a,b). The width of the selvages depends on the size and density of the quartz veins indicating that they are related and that segregation was local with no overall SiO_2 loss into the far field.

Pelitic hornfels-I

The pelitic hornfels-I shows evidence of partial melting with the occurrence of millimetre-scale pockets of leucosome not visible to the naked eye ('metatexites' in the sense used by Droop *et al.*, 2003; Johnson *et al.*, 2003a). They occur always close to the most leucocratic intrusive rocks of the Susqueda igneous complex. The

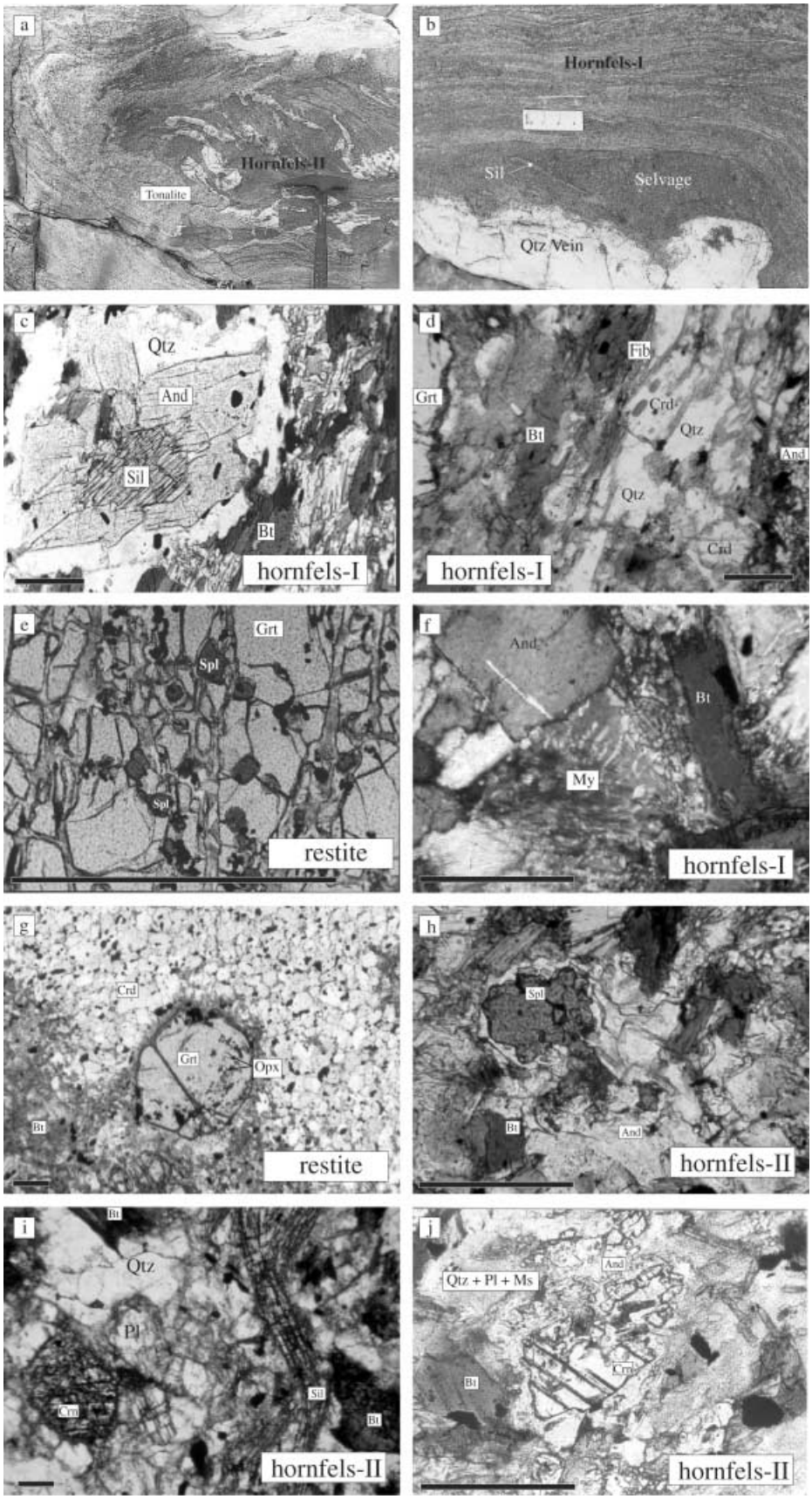

Table 1. List of mineral assemblages in the host rocks and in the regional schists.

Sample	And	Sil	Crd	Grt	Bt	Ms	Qtz	Pl	Crn	Spl	St	Ep	Ap	Opx	Zr	Trm	Ilm	Chl
Micaschists																		
MR-99-14-1	X		X		X	X	X										X	
MR-99-14-2	X		X		X		X									X	X	
MR-99-2	X				X	X	X										X	
MR-99-7-1	X		X		X	X	X										X	
MR-99-7-2	X		X		X	X	X										X	
MR-99-8	X				X	X	X	X				S					X	S
GI-94-2	X				X	X	X				X						X	
Hornfels-I																		
MR-99-24	X	X	X	X	X	S	X	X								X	X	
MR-99-30	S	(f)	X	X	X	S	X	X					X			X	X	
MR-99-36	**1**	**4**	**40**	**3**	**18**	**4_S**	**19**	**9**									**2**	
MR-BR-2	S	X	X	X	X	S	X	X				S	X		X	X	X	
MR-BR-3	S	X	X	X	X	S	X	X					X		X	X	X	
MR-99-13-2	X	(f)	X		X	S	X	X				S					X	S
MR-99-29	X	(f)	X		X	S	X	X									X	
MR-99-34	X	X	X		X		X										X	
MR-99-9	X	X	X		X		X											
Hornfels-II																		
MR-99-22-1	X	(f)	X		X		S	X		X		S				X	X	S
MR-99-22-1b	X	(f)	X		X	S	X S	X		X		S					X	
MR-99-22-2	X	(f)	X		X	S	X S	X		X		S				X	X	
MR-99-25-1	X	X	X		X		S	S	X								X	
MR-99-25-2	X	X	X		X	S	S	S	X									
MR-99-25-3	**15**	**7**	**24**		**26**	**2_S**	**5**	**15**	**2**	**1**						**1**	**2**	
MR-99-25-4		X	X		X	S	S	X S	X	X						X	X	
MR-99-34	X	X	X		X		S	X		X								
Restites																		
MR-98-17	S		X	X	X		X										X	S
MR-98-10	S		X	X	X		X										X	
MR-98-13	S		X	X	S		X										X	
MR-98-15	S		X	X			X										X	S
MR-98-15	S		X	X	S		S			X							X	
MR-98-24			X	X	S					X			X				X	
MR-98-5	S		X	X	X S		S	X		X			X	X	X		X	
MR-98-6a	S		X	X	X S		S	X		X			X	X	X		X	
MR-98-6b			X	X	X S		S	X		X			X	X	X		X	
MR-98-14	X		X		X	S	X										X	

X = interpreted to be part of the peak assemblage; *S* = interpreted to be a secondary later phase; *(f)* = sillimanite present only as fibrolite. The two bold lines list modal proportions of phases from point counting for samples MR-99-36 and MR-99-25-3 that are also used to construct the pseudosections on Figs 6 & 8. 1000 points were counted for each of these thin sections.

rocks preserve relict layering with alternating more psammitic and quartz poor pelitic layers. Tight D2 folds may be preserved. The microstructure is always randomly oriented with syn-post tectonic porphyroblasts overgrowing the older fabric. A typical peak assemblage is biotite + cordierite + plagioclase + aluminosilicate + quartz with or without garnet. Peak assemblages vary with bulk composition. Table 1 lists assemblages of several characteristic samples of hornfels-I with typical modal proportions for a sample later used for the construction of a relevant pseudosection. Coarse-grained aluminosilicate occurs in many but not all samples. Where present, prismatic sillimanite is often overgrown by massive andalusite (Fig. 4c). Andalusite (about 1%) occurs both as inclusion-free euhedral porphyroblasts with inclusions of randomly oriented biotite as well as subhedral inclusion-free crystals. The inclusion-free crystals have pink cores due to their high Fe^{3+} content and are always associated with the quartz-plagioclase rich leucosome pockets.

Fig. 4. Outcrop photos and photomicrographs of rocks and reaction microstructures of the Susqueda contact aureole. (a) Detail of the contact between hornfels-II and a tonalite. Note the density of quartz veins in the host rock. (b) Quartz vein surrounded by silica depleted selvages containing up to 5 cm long sillimanite crystals. The surrounding pelitic hornfels-I shows relict banding. The scale bar is 3 cm. (c) Sillimanite transformed into andalusite in a leucosomic pocket in the pelitic hornfels-I. Similar reaction microstructures occur in hornfels-II. (d) Garnet bearing pelitic hornfels-I. In the right side of the photomicrograph there is a quartz-rich leusosome with euhedral cordierite that contains relic biotite inclusions. Garnet is partially resorbed and has a biotite + fibrolite corona. (e) Spinel inclusions in a garnet core from a restite. (f) Myrmekite (My) probably pseudomorphed after K-feldspar. Biotite shows symplectitic intergrowths with plagioclase. (g) Cordierite-rich restite with orthopyroxene inclusion-rich garnet. The oxide phase is ilmenite. Biotite is present around garnet. (h) Anhedral relic spinel wrapped by andalusite in a silica-undersaturated hornfels-II. (i) Corundum in a trondhejmitic leucosome in hornfels-II. Sillimanite is also observed in the right side of the leucosome. Both sillimanite and corundum are interpreted to have formed peritectically (see text). Corundum has a narrow aluminosilicate rim where in contact with quartz. (j) Anhedral relict corundum wrapped by andalusite in a fine-grained quartz, plagioclase and muscovite leucosome. Scale bar for photomicrographs is 1 mm.

Cordierite occurs as euhedral crystals and constitutes up to 40% of the rock volume. Where in contact with quartz, cordierite has well-developed crystal faces (Fig. 4d) and may contain anhedral relic biotite inclusions. Retrograde fibrolite may overgrow euhedral cordierite. Garnet occurs in Fe-rich varieties of hornfels-I. Garnet is often partially resorbed (Fig. 4d), surrounded by biotite rims and contains inclusions of biotite and ilmenite. In contrast, garnet in more psammitic rocks is rich in concentrically oriented quartz inclusions. Quartz is scarce in many samples and very often it is restricted to quartz-plagioclase leucosome pockets that are interpreted as former melt. Much of the quartz is therefore interpreted as a retrograde phase. Plagioclase overgrows euhedral cordierite crystals and subhedral biotite. Up to 4% of secondary muscovite is associated with myrmekite (Fig. 4f). Tourmaline has been observed in some samples overgrowing euhedral cordierite. Fine-grained ilmenite is a common accessory phase in all samples and shows alignments parallel to the remnant schistosity.

SiO_2 undersaturated hornfels-II

Hornfels-II occurs in the same zone as hornfels-I, but is always associated with the quartz veins (Fig. 4a,b). Hornfels-II is characterized by corundum and spinel-bearing assemblages (Fig. 4h,i). A typical assemblage is sillimanite/andalusite + cordierite + biotite ± corundum + spinel + plagioclase + quartz. Although up to 5% quartz may be present in these rocks it occurs only as minor overgrowths over other phases. Prismatic sillimanite is up to several centimetres in length (Fig. 4b) and it is often replaced by andalusite. Andalusite occurs as subhedral porphyroblasts and is also rimming corundum and spinel (Fig. 4h). Biotite is abundant (25%). It is anhedral and has a deep brown colour. Rutile exsolutions in biotite are common. Cordierite is roughly as abundant as biotite (24%) but altered to pinite in most samples and is intergrown with biotite in the corundum-bearing assemblages. Quartz and plagioclase form leucosomes that are generally not connected although they form millimetre-wide veins in some cases. Hercynitic spinel occurs as anhedral crystals included always in andalusite porphyroblasts. There is typically about 2% corundum in these rocks which occurs within leucosomic halos and is up to several millimetres in size. Corundum is partially replaced by andalusite and white mica (Fig. 4i,j). Ilmenite, galena and sphalerite occur as accessory phases.

Restites

The restites occur in the innermost part of the Susqueda aureole, typically in association with quartz-diorite or as rafts within the igneous complex (Fig. 3b). The rock is granoblastic with a cordierite-rich assemblage characteristic of many low-*P* contact aureoles (e.g. Droop *et al.*, 2003; Johnson *et al.*, 2003a). The two most common assemblages are: cordierite + garnet ± biotite ± spinel ± orthopyroxene ± aluminosilicate + ilmenite and cordierite + garnet + quartz ± biotite + ilmenite. Note that the first assemblage is quartz absent. Cordierite is commonly fresh and forms a fine-grained homogeneous matrix that can constitute 60–90% of the rock volume (Fig. 4g). Round ilmenite inclusions are common. In quartz absent assemblages, spinel inclusions occur in cordierite. Biotite is scarce and occurs as an interstitial phase between garnet grains and surrounding cordierite. Garnet is medium-grained and its distribution in the rock is heterogeneous. It is concentrated close to the restite contacts with the surrounding igneous rocks and may contain relic inclusions of spinel (Fig. 4e) or orthopyroxene (Fig. 4g). Undifferentiated aluminosilicate occurs as an interstitial secondary mineral and it can only be identified using the electron microprobe.

Intrusive rocks

The rocks in the intrusive complex include: (i) Small ultramafic cumulates; (ii) Quartz bearing gabbros and quartz-diorites with the assemblage plagioclase + quartz + hornblende, with or without biotite. These rocks are particularly abundant in the core of the igneous body and contain $<20\%$ quartz; (iii) Tonalites to trondhjemites with the assemblage plagioclase + quartz + biotite. These rocks are more abundant towards the outer part of the complex near the contact with the country rocks. The modal abundance of quartz and plagioclase in these rocks is substantially higher than in the diorites. Plagioclase in all intrusive rocks shows a concentric zonation and is often altered to sericite in its core. Quartz is interstitial between plagioclase. Biotite and amphibole occur in bands oriented within the magmatic foliation. Biotite is subhedral, can be partially chloritized and contains zircon and/or monazite inclusions. Muscovite is present as a secondary phase and may partially replace biotite. Brown-greenish amphibole occurs as prismatic crystals up to 2 cm in length. Amphibole can show concentric zonation from brown in the core to green in the rim.

The contacts between the igneous rock and the metapelitic host rocks are rarely well defined but have a range of interesting features. Contacts between igneous rock and restite occur nearer the centre of the complex (Fig. 3b). Contacts of the igneous rock with hornfels-I occur usually in the most distal and leucocratic (tonalite) parts of the aureole. In some of these contacts the hornfelses appear as schlieric xenoliths (Mehnert, 1968). In the most leucocratic samples, anhedral andalusite xenocrysts occur that are wrapped by a fine muscovite rim. Similarly, garnet and subhedral cordierite are often present within the igneous rock. Accessory igneous minerals are zircon and apatite.

Table 2. Major element whole-rock data for host and intrusive rocks.

Sample	Micaschists							Hornfels-I						Hornfels-II			Restites					Susqueda igneous complex			
	G-241	G-245	Gi-95-4	G-297	G-268	99-14f	99-14b	99-24	Br-3	Br-2	99-36	99-30	99-34f	99-22	99-25-3	99-34b	98-7	98-24	98-6	98-5	98-25	98-24	98-4	99-25	Br-1
SiO_2	66.06	57.10	64.06	54.97	57.33	60.68	61.64	52.89	50.09	50.79	48.79	46.16	43.73	47.07	42.44	42.37	43.17	41.68	43.36	43.86	46.05	48.13	50.28	56.89	63.50
TiO_2	0.85	0.06	0.94	1.00	0.93	1.13	1.21	1.40	1.50	1.77	1.56	1.91	1.98	1.66	1.66	1.43	2.26	2.46	2.16	2.19	1.90	1.05	1.62	1.45	0.92
Al_2O_3	16.04	22.50	17.97	20.90	21.64	18.46	19.42	23.14	22.92	21.56	24.82	26.36	26.87	26.87	32.07	30.59	25.40	26.95	25.72	29.06	26.25	21.38	19.41	18.52	17.11
FeO	6.77	8.33	8.68	9.10	8.24	7.55	7.23	8.86	10.97	12.44	11.52	13.85	15.05	11.27	10.04	11.83	12.33	13.22	12.58	14.03	13.87	11.80	10.30	8.70	5.33
MnO	0.05	0.06	0.05	0.09	0.06	0.04	0.04	0.06	0.07	0.10	0.11	0.10	0.12	0.15	0.10	0.09	0.14	0.16	0.15	0.18	0.10	0.11	0.19	0.12	0.04
MgO	2.05	2.14	1.63	3.65	2.33	1.95	1.89	2.60	3.30	3.54	3.73	4.18	4.56	2.92	2.82	3.16	5.26	6.00	5.30	6.83	4.26	6.04	5.03	3.05	1.51
CaO	0.83	0.55	0.94	0.80	0.35	0.38	0.24	0.64	1.60	0.58	0.54	0.45	0.31	0.28	0.81	1.08	3.79	2.79	3.76	0.72	0.44	5.41	7.23	5.92	3.00
Na_2O	2.31	1.91	1.49	1.75	1.68	1.46	0.78	1.31	1.99	0.67	0.58	1.58	1.10	0.49	0.91	1.93	0.81	0.64	0.89	0.41	1.44	0.95	2.26	3.53	3.72
K_2O	3.78	3.59	3.31	4.31	4.24	3.46	2.32	3.35	3.23	3.42	3.36	2.97	2.97	3.73	3.35	3.52	1.62	1.42	1.65	1.29	2.99	1.06	1.17	0.58	1.15
P_2O_5	0.00	0.00	0.00	0.00	0.00	0.16	0.19	0.18	0.15	0.23	0.13	0.00	0.00	0.23	0.21	0.00	0.11	0.08	0.10	0.02	0.00	0.13	0.00	0.00	0.29
Total	98.74	96.24	99.07	96.57	96.80	95.27	94.96	94.43	95.82	95.10	95.14	97.56	96.69	94.67	94.41	96.00	94.89	95.40	95.67	98.58	97.30	96.06	97.49	98.76	96.57
X_{Al}	0.65	0.68	0.64	0.62	0.67	0.66	0.68	0.67	0.62	0.57	0.62	0.59	0.58	0.65	0.71	0.67	0.59	0.58	0.59	0.58	0.59	0.55	0.56	0.61	0.71
X_{Fe}	0.77	0.80	0.84	0.71	0.78	0.79	0.79	0.77	0.77	0.78	0.76	0.77	0.77	0.79	0.78	0.79	0.70	0.69	0.70	0.67	0.77	0.66	0.67	0.74	0.78
X_{Si}	0.73	0.63	0.69	0.62	0.64	0.68	0.68	0.60	0.57	0.57	0.55	0.51	0.48	0.53	0.49	0.48	0.50	0.47	0.50	0.47	0.51	0.55	0.59	0.65	0.73
X_{KN}	0.21	0.15	0.15	0.17	0.17	0.16	0.10	0.13	0.13	0.11	0.10	0.10	0.09	0.10	0.09	0.11	0.06	0.05	0.06	0.04	0.10	0.06	0.10	0.13	0.18

Whole-rock geochemistry

The X-ray fluorescence (XRF)-derived bulk compositions of the pelitic hornfels-I, restites and silica-undersaturated hornfels-II differ not only in silica content but also with respect to several other elements (Table 2; see Appendix for analytical methods). Hornfels-I and -II show similar molar $X_{Fe} = FeO/(FeO + MgO)$ ratios with $X_{Fe} = (0.76–0.78)$ for hornfels-I and $X_{Fe} = (0.78–0.79)$ for hornfels-II. Both are in the range of most of the pelitic schists with $X_{Fe} = (0.77–0.80)$. However, the restites appear to be depleted in FeO ($X_{Fe} = 0.67–0.77$). The composition of the staurolite bearing micaschist has lower magnesium content MgO = 1.63 wt% than other micaschists MgO = (1.95–3.65 wt%). This result suggests that the occurrence of the staurolite bearing assemblage is not caused by different P–T conditions but a higher FeO content of the bulk. A comparison of the $X_{Al} = Al_2O_3/(Al_2O_3 + FeO + MgO)$ suggests a depletion in alumina in hornfels-I ($X_{Al} = 0.58–0.62$) relative to the micaschists ($X_{Al} = 0.62–0.68$) (Fig. 5).

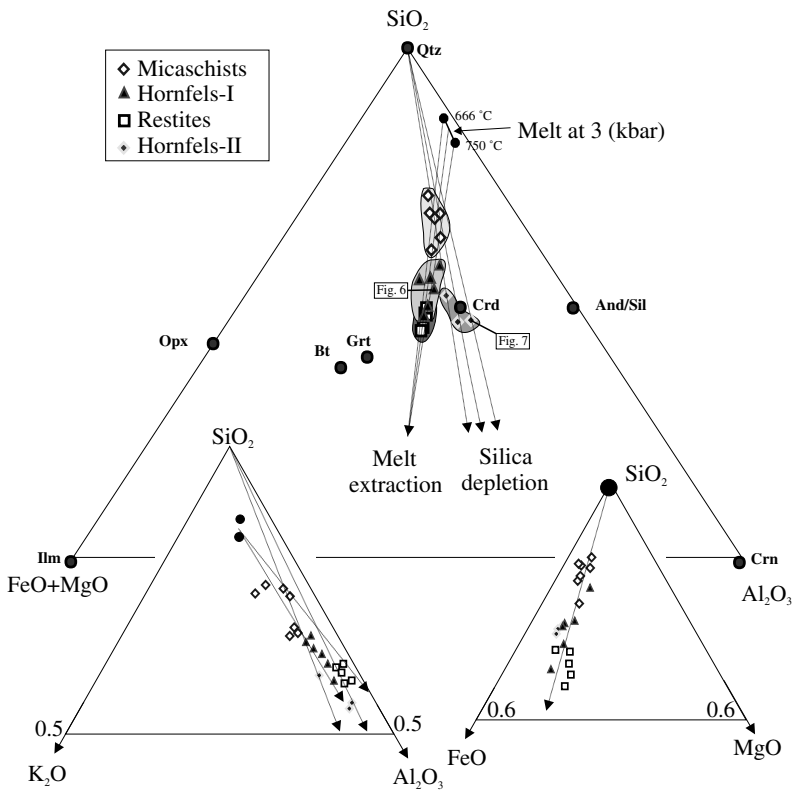

Fig. 5. Relationship between SiO_2, Al_2O_3 and FM = (FeO + MgO + TiO_2 + MnO) of bulk compositions of the different rock types in comparison with a calculated equilibrium melt composition (black dots shown in the top right side of the diagram). The end points of the small melt bar are for a melt composition at the solidus (666 °C, 3 kbar): H_2O:SiO_2:Al_2O_3:CaO:MgO:FeO:K_2O:Na_2O = 23.5:64.3:6.4:0.2:0.0:0.1:3.0:2.4 and at 750 °C, 3 kbar: H_2O:SiO_2:Al_2O_3:CaO:MgO:FeO:K_2O:Na_2O = 18.4:65.0:8.3:0.5:0.2:1.0:4.4:2.1 All oxides are plotted in weight per cent. The trends are supported by the trends in the SiO_2:Al_2O_3:K_2O diagram in the large inset at left and the SiO_2:MgO:FeO diagram in the small inset at right. See text for details.

This depletion is more evident in the restites (X_{Al} = 0.58–0.59). In contrast, the alumina ratio in hornfels-II is considerably higher (X_{Al} = 0.67–0.71). The silica depletion $X_{Si} = SiO_2/(SiO_2 + Al_2O_3 + FeO + MgO)$ is evident in all rock types in the Susqueda aureole. In comparison with the majority of micaschists (X_{Si} = 0.60–0.73), hornfels-I has lower X_{Si} with values between 0.48 and 0.57, as well as both hornfels-II (X_{Si} = 0.48–0.53) and restites (X_{Si} = 0.47–0.51).

These relationships are consistent with a model of successive melt loss. This can be illustrated using a ternary Al_2O_3–(FeO + MgO + TiO_2 + MnO)–SiO_2 (A–FM–S) diagram (Fig. 5). Assuming the bulk composition of the micaschist as a protolith, two important trends are defined: silica depletion causes a linear change from the SiO_2 apex through the precursor rock to lower SiO_2contents. Depletion vectors retain constant A/(A + FM) ratios, consistent with the formation of the hornfels-II. Correspondingly, melt depletion causes a linear change from the composition of the melt through the precursor composition. The composition of an equilibrium melt calculated at 3 kbar is plotted on the diagram. Vectors from this composition through the precursor rocks trend towards the composition of hornfels-I and further towards the restites. From these relationships it is hypothesized that hornfels-I and the restites formed due to successive depletion of melt from the micaschists, while the silica-undersaturated hornfels-II is only depleted in silica (during the preanatectic quartz vein forming event), but has lost no melt.

While this interpretation is consistent with Fig. 5, it is noted that this figure is not a projected compatibility diagram, but simply a comparison of three selected components of the bulk rock composition as determined by XRF analysis (Table 2). As such, it needs to be shown that the interpretation of Fig. 5 is robust towards the changes of the other components. The insets in Fig. 5 show that the model is supported by the trends of K_2O: hornfels-I and restites are more depleted in K_2O than hornfels-II and the two rock groups lie on corresponding compositional vectors with melt and with the SiO_2 apex, respectively. In view of the alkali content of the partial melt, the model is further supported by the $X_{KN} = (K_2O + Na_2O)/(K_2O + Na_2O + Al_2O_3 + FeO + MgO)$. The ratios of X_{KN} in the micaschists (X_{KN} = 0.15–0.21) are higher than that in hornfels-I (X_{KN} = 0.09–0.13). The restites have the lowest alkali contents (X_{KN} = 0.04–0.10). Hornfels-II is also somewhat depleted in alkalis (X_{KN} = 0.09–0.11) but it is suggested that this alkali depletion there occurred during the vein segregation prior to the contact metamorphic event described here. A bulk composition in the selvages around quartz veins is also included in the analyses (Sample 99–14b) and also a composition from the same schist out of the selvage. The comparison of both bulk compositions shows that the rocks are depleted in K_2O and Na_2O in the selvages (X_{KN} = 0.16 in the schist to X_{KN} = 0.10 in the selvage). It is concluded that the bulk compositions of hornfels-I and restites are consistent with a derivation from the micaschists by successive melt loss and that hornfels-II was derived from the micaschists by the segregation of silica and some alkalis during a preanatectic event. In the remainder of this paper this hypothesis is tested using the grid in Fig. 2 and several thermodynamic pseudosections.

APPLICATION OF PHASE DIAGRAMS TO PARTIAL MELTING IN THE SUSQUEDA AUREOLE

In order to test if the grid shown in Fig. 2 can be used to explain the Susqueda aureole equilibrium *P–T* pseudosections for hornfels-I and -II were constructed. It is planned to test if the hornfelses and the restites can be explained as derivates from the host rocks as suggested above. In order to perform this test in a realistic system, these pseudosections were calculated in the NCKFMASH system, and it is shown that these phase diagrams can be related to the *P–T*, KFMASH projection shown in Fig. 2. Because of our observation that andalusite-sillimanite equilibria occur in the vicinity of the solidus (e.g. Fig. 4c) we have followed the logic of Johnson *et al.* (2003b)) and increased the enthalpy of formation of sillimanite by 0.25 kJ mol^{-1} in the data set of Holland & Powell (1998), thus allowing for a larger stability field for andalusite.

Formation of hornfels-I and restites

Silica-saturated melting during the formation of hornfels-I and restites is studied using pseudosections appropriate to the evolution of hornfels-I. Two pseudosections were calculated. Figure 6 is a *P–T* pseudosection for the bulk composition of hornfels-I sample MR-99-36 (using the XRF analysis of Table 2 recalculated to mol.%). As this diagram is isochemical, a T–X_{melt} pseudosection is then discussed in Fig. 7 which can be used to test the melt extraction model hypothesised above.

In order to construct a pseudosection for sample MR-99-36, a water content has to be estimated for the bulk composition. In the absence of any constraints on this, a H_2O content was assumed that suffices to have a water saturated solidus in the complete pressure range considered in Fig. 6. This is about 2% H_2O. Using this water mode, there is only one point in Fig. 6 – at about 3.5 kbar – where the complete consumption of water occurs exactly at the solidus. In addition to the phases considered in Fig. 2, staurolite and plagioclase are also considered so that we now consider the 13-phase system staurolite, garnet, orthopyroxene, cordierite, spinel, K-feldspar, biotite, muscovite, plagioclase, aluminosilicate, quartz, corundum and liquid. Quartz is not assumed to be in excess. Several of the narrow divariant fields shown in Fig. 6 can be related to reactions in the KFMASH *P–T* projection (Fig. 2). For example, the NCKFMASH divariant field Grt +

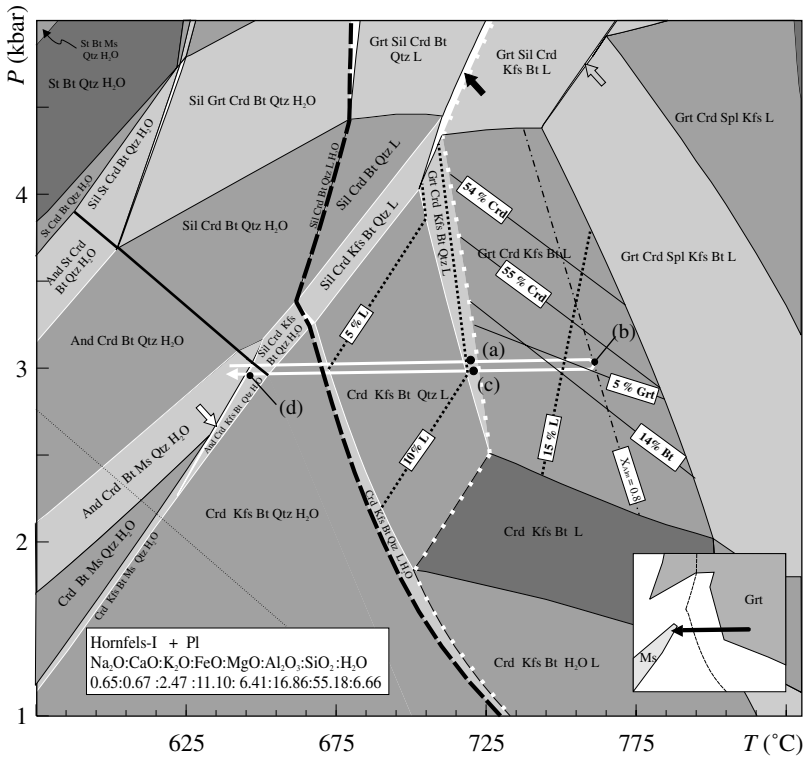

Fig. 6. *P–T* pseudosection in NCKFMASH for hornfels-I (using the bulk composition from sample MR-99-36; Table 2). H_2O content was estimated to saturate the solidus up to 5 kbar. Divariant fields are white and shading decreases with increasing variance. The solidus is marked by the black dashed line. The quartz out boundary is marked by the white dotted line. The inset shows the stability regions of garnet and muscovite. Black and grey arrows refer to corresponding equilibria on Fig. 2. Modal isopleths for melt (dotted line) and several solid phases (solid lines) are drawn in the quadrovariant peak field Grt + Crd + Ksp + Bt + L + Pl.

Sil + Crd + Bt + Pl + Kfs + Qtz + L (black arrow in Fig. 6) is the equivalent of the KFMASH reaction Sil + Bt + Qtz = Grt + Crd + Kfs + L (black arrow in Fig. 2). Similarly, the quartz absent divariant Grt + Sil + Crd + Spl + Kfs + Bt + Pl + L (grey arrow in Fig. 6) corresponds to the KFMASH reaction Bt + Grt + Sil = Crd + Spl + Kfs + L in Fig. 2 (grey arrow) and the divariant And + Crd + Kfs + Bt + Ms + Pl + Qtz + H_2O (white arrow in Fig. 6) relates to the KASH univariant Ms + Qtz = And + Kfs + H_2O (Fig. 1). Note that the addition of Na_2O and CaO shifts melt bearing reactions to some 50 °C towards lower temperatures.

Hornfels-I is well-constrained on this pseudosection (Fig. 6). The sample MR-99-36 contains the assemblage: cordierite (overgrown by fibrolite) + garnet + biotite + quartz + plagioclase with secondary muscovite and andalusite (Table 1). From field geological arguments on the contact metamorphic nature of the hornfelses it is reasonable to assume that the *P–T* path is characterized by isobaric heating and cooling. The pressure of this *P–T* path is constrained by the occurrence of garnet and retrograde muscovite. Garnet only occurs above 2.5 kbar and the highest pressure of retrograde muscovite formation is about 3–3.5 kbar (see inset in Fig. 6). It is therefore suggested that the *P–T* path evolved at 3 ± 0.5 kbar. At 3 kbar, garnet first appears as a peritectic phase around 720 °C in the trivariant reaction: Bt + Pl + Qtz = Grt + Crd + Kfs + L (labelled (a) in Fig. 6). This is consistent with garnet often occurring in association with leucosomes. The contact metamorphic peak is reached within the quadrivariant field Grt + Crd + Kfs + Bt + L (+Pl) during the massive production of cordierite due to further incongruent melting. Modal contours for the most abundant peak phases biotite, cordierite and garnet in Fig. 6 are roughly consistent with point counting estimates for this sample as shown in Table 1. (Note that all contours shown on the pseudosections are mole per cent normalised to one oxide and must be converted to volume per cent for direct comparison. However, in view of the uncertainties associated with equilibration volume a detailed such comparison is not warranted and modal contours on pseudosections can only give a ballpark estimate of those observed in thin section). Thus, it is suggested that the peak temperature can realistically only be constrained to lie between 735 °C and 775 °C. Nevertheless, a peak temperature around 760 °C is labelled as (b) in Fig. 6 on the basis of garnet core composition (see Appendix). Retrograde resorption of garnet to biotite occurred at (c) which is also observed in thin section (Fig. 4d). Simultaneously, K-feldspar and melt are consumed to form biotite. Finally, retrograde formation of fibrolite and later andalusite form at (d). Formation of retrograde muscovite on the expense of final K-feldspar also occurred at this temperature. However, the parageneses in the sub solidus region of Fig. 6 are inconsistent with the micaschist parageneses of the supposed precursor of hornfels-I and muscovite modes in Fig. 6 are much smaller than retrograde muscovite mode observed in thin section (no muscovite modes are shown in Fig. 6,

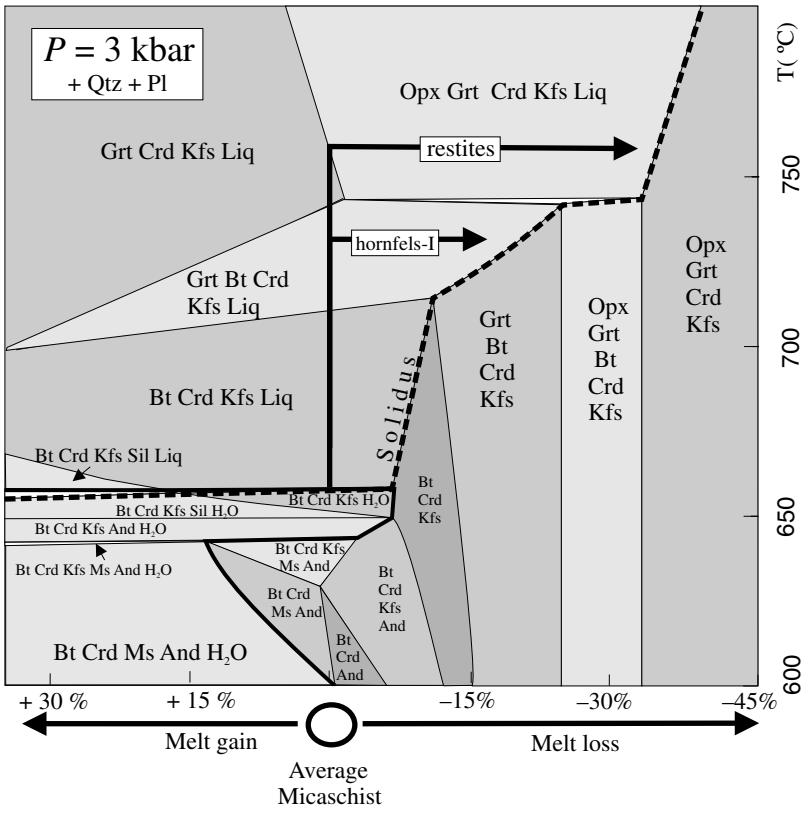

Fig. 7. T–X_{melt} pseudosection at 3 kbar with X_{melt} being the melt mode in mol.%. The starting composition in the centre (black circle) is an average micaschist, averaged from the analyses in Table 2 and recalculated to mol.%. This composition of the average micaschist in terms of oxides is: H_2O:SiO_2:Al_2O_3:CaO:MgO:FeO:K_2O:Na_2O = 4.95:66.89:12.80:0.69:3.70:6.68:2.53:1.74. Composition of the melt extracted is calculated for a melt in equilibria with the average bulk at 750 °C and 3 kbar is: H_2O:SiO_2:Al_2O_3:CaO:MgO:FeO:K_2O:Na_2O = 14.95:63.31:14.18:0.20:0.26:1.25:3.39:2.45. The solidus is drawn as the thick dashed line. The water saturation line is a thick solid line.

but point (d) is very near the muscovite-out boundary, so that its mode is very small). This is because the evolution of these rocks was associated with partial melt loss and possibly later melt-reintegration and they cannot be interpreted on an isochemical pseudosection.

How much melt?

Figure 6 indicates that there was about 15% melt in the rock at the metamorphic temperature peak. However, this melt mode is a strong function of the somewhat arbitrarily assumed H_2O content of the bulk composition (Guiraud *et al.*, 2001). In fact, at the relevant pressure of 3 kbar about 5% of melt form on the expense of water within 4 °C above the solidus. Considering that all water successively liberated during the prograde evolution is likely to leave the rock (Spear *et al.*, 1999; Guiraud *et al.*, 2001), it is more probably that the solidus and the complete consumption of water occur at a water activity of 1 at almost the same temperature. This implies that the melt mode shown in Fig. 6 for the metamorphic temperature peak is an overestimate. Moreover, extraction of melt during the prograde evolution implies that the evolution of hornfels-I did not occur isochemically and must be considered on an appropriate T–X section (e.g. White & Powell, 2002).

Figure 7 shows a T–X_{melt} pseudosection with temperature on the vertical axis and melt mode on the horizontal axis. The central bulk composition labelled with the circle is an average bulk composition of the micaschist samples from Table 2. The water content of the bulk composition (just under 5%, see Fig. 7) was chosen so that the solidus of the average micaschist is just water saturated. It may be seen that typical parageneses of the regional micaschists are predicted in the low temperature part of this diagram. At 735–750 °C the peak parageneses of hornfels-I and the restites are also predicted. Extraction of some 15% of melt at a metamorphic peak temperature around 735 °C for hornfels-I shows that the peak parageneses Grt + Crd + Bt + Pl + Qtz + Kfs can be explained and also preserved during subsequent cooling. Restites form closer to the intrusion (Fig. 3b) where the contact metamorphic peak may have been even higher. At 750 °C orthopyroxene bearing parageneses are predicted and preserved after extraction of some 30% melt. The extraction of substantial portions of melt is also reflected by the fact that only small pockets of leucosomes are observed in the field in both hornfels-I and the restites. Figure 7 also shows that all phase fields are quartz saturated in the considered temperature range. This is in contrast with the pseudosection in Fig. 6, but reflects the observations better: Complete consumption of quartz near or above the metamorphic peak conditions is

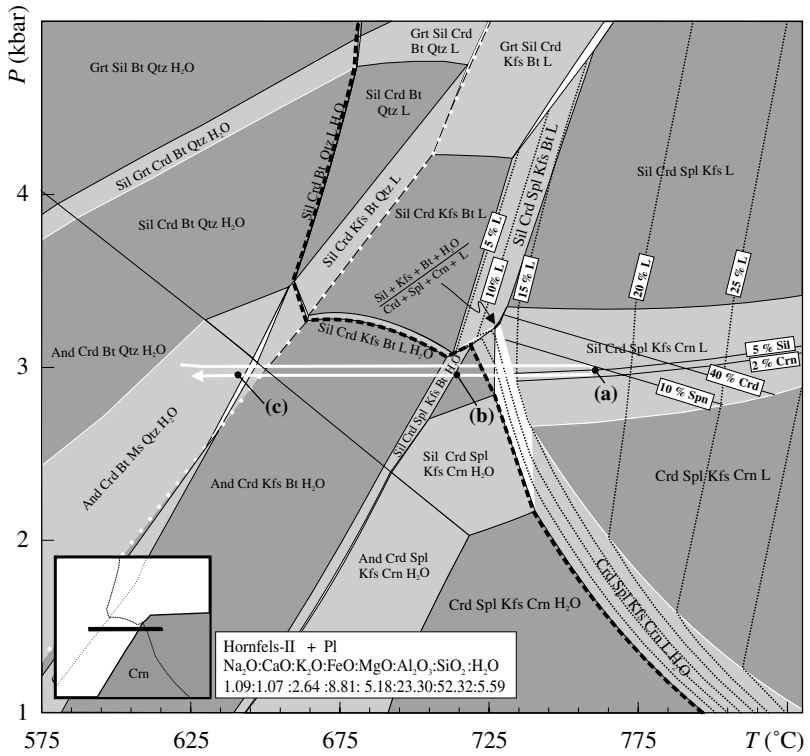

Fig. 8. *P–T* pseudosection for the silica-undersaturated hornfels-II sample MR-99-25-3 but FeO was corrected from Table 2 by ilmenite. For other details see caption of Fig. 6. The inset shows the stability field of corundum.

indicated by the occurrence of both silica-saturated and silica-undersaturated parageneses in hornfels-I. Figure 7 also has an interesting prediction for the leucosomes: the solidus on the left side of the average micaschist, i.e. in the region of melt gain, occurs in the presence of aluminosilicate. This is observed in several rocks in thin section (i.e. Fig. 4c,i). It is concluded that between 15 and 30% of melt were extracted from hornfels-I and the restites during their prograde evolution.

SiO_2 undersaturated hornfels-II

Silica-undersaturated melting in hornfels-II is studied on a *P–T* pseudosection appropriate to sample MR-99-25-3 (Tables 1 & 2). However, in view of substantial quantities of ilmenite (*c*. 4%) in this sample, Fe was reduced from the XRF analysis by a number of cations corresponding to Ti. The amount of Ti bound in biotite was omitted since the model does not include Ti. In comparison to the bulk composition used for Fig. 6 this bulk is more Al_2O_3 rich, contains less SiO_2 and somewhat less FeO and MgO. As for Fig. 6, the H_2O content of the bulk composition was initially adjusted so that the solidus is just water saturated across the entire pressure range considered in Fig. 8 (note that the water saturation line touches the solidus at 3.5 kbar only).

The pseudosection is similar to that in Fig. 6 in the quartz saturated area (left of the dotted white line). All divariant fields discussed above and related to Fig. 2 also appear in Fig. 8. Other reaction spaces in the silica-saturated region are also equivalent. However, in contrast to Fig. 6 the quartz saturation line intersects the solidus around 3.2 kbar. As a consequence, a range of silica-undersaturated parageneses occur below the solidus at low pressures. Three distinct sections of the solidus can be discerned: (i) above 3.2 kbar, the quartz saturated solidus has a positive slope and melting occurs in a similar fashion to that illustrated for silica-saturated rocks in Fig. 6; (ii) between 3 kbar and about 3.2 kbar the solidus is near isobaric and melting can only be produced by a pressure increase. This part of the solidus is both quartz and corundum absent and corresponds to the KFMASH univariant reaction Crd + Spl + Kfs + H_2O = Sil + Bt + L (see Fig. 2); (iii) below about 3 kbar the solidus is formed by an incongruent melting reaction derived from the KFMASH univariant reaction Sil + Crd + Spl + Kfs + H_2O = Crn + L (Fig. 2). The reaction causes formation of peritectic corundum. The strong kink between the lower and upper parts of the solidus is caused by its intersection with the quartz saturation line: as melt contains high percentage of SiO_2, silica-undersaturated melting commences at much higher temperatures than silica-saturated melting.

The evolution of hornfels-II in Fig. 8 supports the *P–T* evolution inferred for hornfels-I in Fig. 6. Hornfels-II sample MR-99-25-3 has the assemblage cordierite + aluminosilicate (andalusite as overgrowths corundum and spinel) + plagioclase + quartz (also as myrmekites with plagioclase and muscovite) + corundum and spinel (as relics constituting *c*. 2 vol.%) + biotite (as late intergrowths with cordierite) (see Table 1; Fig. 4h,j and Petrography section). The

formation pressure suggested for hornfels-I to be around 3 kbar is confirmed by the hornfels-II parageneses: Corundum occurs only at pressures below 3.2 kbar and peritectic sillimanite only occurs at pressures above 2.5 kbar (Fig. 8, inset). Both corundum and sillimanite occur as euhedral crystals in leucosomes of hornfels-II and are interpreted as peritectic phases. Peak metamorphic conditions are therefore well-constrained to lie in the trivariant field Sil + Crd + Spl + Kfs + Crn + L above 725 °C at 3 kbar (labelled (a) in Fig. 8). Modal contours within this field are not very temperature dependent, but roughly confirm that peak conditions were reached within this field. The biotite-cordierite intergrowths observed in thin sections are interpreted as retrograde reactions between the solid phases and melt during cooling at (b). It is also suggested that the trivariant reaction near (b) causes retrograde consumption of K-feldspar. The final consumption of K-feldspar occurs at temperatures around 640 °C in the divariant field producing muscovite and plagioclase-quartz myrmekites on the expense of K-feldspar at (c). The source of the late H_2O required for this back reaction is inferred to be derived from magma crystallization.

The amount of melt produced during the evolution of hornfels-II is much smaller than for hornfels-I: the solidus at 3 kbar occurs at 730 °C (near the metamorphic peak) which is some 60 °C higher temperature than for hornfels-I. While the melt modes in Fig. 8 appear to indicate above 15% melt at the metamorphic peak, it is noted that most of this melt is produced within 10 °C of the solidus in the water saturated melting. This is unrealistic and occurs only because the H_2O content of the bulk composition was arbitrarily chosen so that the solidus is water saturated across the entire pressure range of Fig. 8. A refined water content would cause effective initial melting at 3 kbar in the trivariant field Sil + Crd + Spl + Kfs + Crn + L and negligible melt modes at the metamorphic peak. It is suggested that less than 5% melt is a realistic estimate for the melt content of hornfels-II.

DISCUSSION

In the previous sections it was suggested that all hornfelses in the contact aureole experienced a similar thermal evolution at 3 kbar, but that the pelitic hornfels-I has melted substantially more (and lost substantially more melt) than the silica-undersaturated hornfels-II. In order to summarize this interpretation and to show how rocks with different quartz contents can cause silica-saturated *v.* silica-undersaturated melting, a T–X_{SiO_2} pseudosection was constructed (Fig. 9). Except for silica and water, the pseudosection was constructed for the bulk composition of hornfels-II (used in Fig. 8). It was shown in Fig. 5 that this rock is equivalent to the precursor micaschists – except for a strongly depleted silica content. In refinement to Figs 6 & 8 the water content was assumed to be in excess below the solidus. Above the solidus, the water content of the bulk composition was assumed to be that of the solid-phase paragenesis at the solidus (Guiraud *et al.*, 2001). As such, the water content of the bulk composition varies horizontally in the melting area and the width of the narrow low-variance fields in which two fluids coexist shrinks to zero. The X_{SiO_2} axis covers a range of SiO_2 contents from that of Fig. 8 at the left hand side to 66 mol.% along the right hand side margin. The average SiO_2 content of metapelites in the micaschists zone is 63%.

This diagram shows the importance of the effect of an early SiO_2 depletion in aluminous pelitic rocks. For quartz bearing rocks the solidus occurs at 670 °C. However, where the quartz saturation line intersects the solidus, it rapidly climbs to 725 °C. Quartz-rich micaschists contain the regional metamorphic assemblage Bt + Crd + Ms + And + Qtz + H_2O at around 625 °C. Contact metamorphic heating causes initial melting at 670 °C and substantial melting while crossing the quadrivariant reaction space Crd + Ksp + Sil + Qtz + L up to the metamorphic peak around 750 °C. The peak assemblage observed in hornfels-I does not match the assemblage of this quadrivariant field because hornfels-I has experienced significant melt loss which we considered in the discussion of Fig. 7. In contrast, segregation of quartz veins during regional metamorphism at around 625 °C has depleted the rocks in silica to around 52% SiO_2. Subsequent contact metamorphic heating forms the assemblages observed in hornfels-II around 750 °C, but is only associated with few per cent melting. This melt may not have been enough to segregate from the rock and is likely to have remained *in situ*. Figure 9 therefore nicely confirms the interpretations from above.

A peculiar observation in all rocks discussed here is that the metamorphic peak assemblage is only preserved in relics and K-feldspar is completely absent, although it is predicted by the pseudosections in Figs 6 & 8. Johnson *et al.* (2003a)) made a similar observation and provided a number of possible explanations. It is suggested here that the absence of K-feldspar at Susqueda can also be explained by the geological situation. A contact metamorphic event overprints a regional metamorphic event that took place largely simultaneously. Figure 9 shows that the paragenesis of the regional micaschists is consistent with temperatures around 625 °C at the time of intrusion of the Susqueda igneous complex and formation of the hornfelses. Thus, cooling from the contact metamorphic event terminated at 625 °C in the vicinity of the K-feldspar breakdown reaction labelled with (c) in Fig. 8. It is suggested that the rocks experienced massive post-peak re-equilibration at this temperature, leaving only relic phases as evidence for the metamorphic peak conditions. This late re-equilibration also explains the substantial back reaction of sillimanite to andalusite.

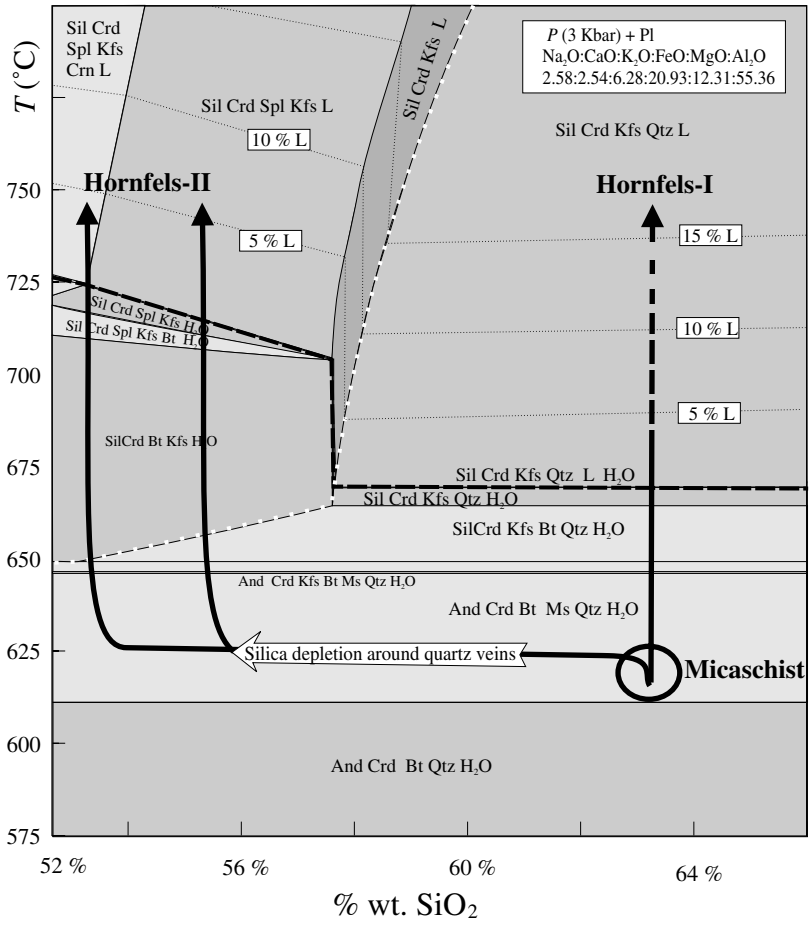

Fig. 9. T–X_{SiO_2} diagram at 3 kbar constructed from the bulk composition used in Fig. 8. Water is assumed to be in excess below the solidus. Above the solidus the water content of the bulk composition is assumed to be that of the solid phase assemblage at the solidus. Thus, no low-variance fields with coexisting H_2O and melt appear near the solidus. The solidus is shown by the black dashed line, the quartz saturation line with the white dotted line. The thick arrow for hornfels-I is dashed towards higher temperatures, as the extraction of melt changes silica content as well. Thus, the upper part of the thermal evolution of hornfels-I is better interpreted in Fig. 7.

Where is the melt?

The hornfels-I and restites can be explained as successively melt depleted products of the micaschists and that hornfels-II experienced comparatively little melting. In contrast, field observations show little evidence for leucosome in both rock types. This poses the question: where is the partial melt extracted from hornfels-I and the restites ? It is suggested here that this partial melt mixed and assimilated with the igneous rocks of the Susqueda complex. This is indicated by several observations: (i) The Susqueda igneous complex is largely composed of diorite and more mafic igneous rocks and is only leucocratic in its outermost parts; (ii) Cordierite and garnet are common in the leucocratic parts; (iii) Tourmaline has been found to cross garnet crystals.

To test this suggestion more rigorously, selected bulk compositions of magmatic rocks of the Susqueda igneous complex are plotted in the A–FM–S diagram previously used in Fig. 5 (Fig. 10). The igneous rocks show a silica enrichment from $X_{Si} =$ 0.55 in the quartz gabbro to 0.71 in the tonalite. The alkali index show a parallel behaviour from X_{KN} 0.06 to 0.18 and the rocks have consequently higher relative X_{Fe} ratios ($X_{Fe} = 0.66$ to 0.71) that trend to those ratios observed in the host rocks. The X_{Al} also increases to the tonalitic rock as an evidence that the rock assimilates more Al_2O_3 relative to the ferromagnesiam components. The CaO wt% also decreases progressively from the gabbro to the tonalite. In

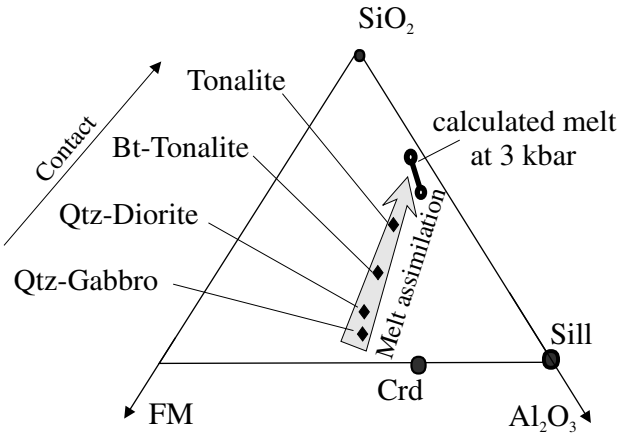

Fig. 10. Comparison of bulk compositions from different rocks from the Susqueda igneous complex in comparison with a calculated equilibrium melt composition as for Fig. 5.

summary, the quartz-gabbros, quartz-diorites and tonalites (spatially from the inner parts of the igneous complex to the outer parts) defined in Fig. 10 a trend towards the same bulk composition that is assumed to be extracted in Fig. 5. This confirms that at least some of the partial melt extracted from the hornfelses and restites mixed with the intruding magma (Droop *et al.*, 2003).

CONCLUSIONS

In conclusion it may be summarized that the rocks in the Susqueda contact aureole show a range of rock types useful for the interpretation of silica-saturated *v.* silica-undersaturated melting of pelites. The regional metamorphic micaschists outside the contact aureole are of cordierite-andalusite metamorphic grade and have highly variable quartz contents due to local segregation of quartz veins. During intrusion of the igneous complex near the time of the regional metamorphic peak, rocks in the vicinity of the contact experienced contact metamorphic migmatisation. This migmatisation is very different for rocks with different quartz contents.

Quartz-rich pelitic precursors reach their contact metamorphic peak at 3 kbar and roughly 750 °C in the stability field of the quadrivariant assemblage Grt + Crd + Kfs + Bt + L + Pl. In the process they metamorphosed to hornfels-I and formed at least 15–20% melt. However, hornfels-I contains only small leucosomic pockets so that it is inferred that most of this melt was lost from the rock. In contrast, quartz-poor pelitic precursors formed a silica-undersaturated hornfels-II and are characterised by peak assemblages including peritectic corundum and sillimanite. These rocks show negligible melting. Melt extraction from hornfels-I and restites, as well as pre-anatectic silica extraction from hornfels-II is nicely confirmed by T–X_{melt} and T–X_{SiO_2} pseudosections, respectively.

This model is also confirmed by bulk compositional trends in an Al_2O_3–SiO_2–(FeO + MgO + MnO + TiO_2) (A–S–FM) diagram. This diagram shows that micaschists, hornfels-I and restites define a compositional trend that is collinear with the composition of an equilibrium melt at 3 kbar. This trend is consistent with a successive melt depletion model to form hornfels-I and restites. In contrast, micaschists and hornfels-II are collinear with the quartz apex, suggesting that these rocks segregated quartz, but did not loose melt.

The melt lost from hornfels-I is interpreted to have assimilated with the igneous rocks of the Susqueda igneous complex to form the tonalitic rocks in the distal parts of the intrusive complex. This is supported by the compositional trends of gabbroic, dioritic and tonalitic rocks from the complex on the (A–S–FM) diagram. This trend (from the centre to the margins of the complex) points towards the equilibrium melt composition of the metapelitic host rocks.

ACKNOWLEDGEMENTS

This work has been carried out in part within a 4-year period during which the first author benefited from a FPI scholarship from Spain's MCYT in the framework of the UAB research project PB97-0198-CO2-01. It also has benefited from the projects BTE2003-08653-C02-01 and Acciones Integradas Hispano-Austriacas HU2000-0024. The study was also supported by project P-15474 of the Austrian Science foundation (FWF) and ÖAD grant 19/2001 for cooperation between Austria and Spain. T. Johnson is thanked for many discussions and for critically reading the manuscript before submission. R. White and M. Guiraud are thanked for careful reviews and R. Powell for some hints during the revision process. D. Robinson is thanked for his always so thorough editorial work.

REFERENCES

Bowers, J. R., Kerrick, D. M. & Furlong, K. P., 1990. Conduction model for the thermal evolution of the Cusuptic aureole, Maine. *American Journal of Science*, **290,** 644–665.

Carrington, D. P. & Harley, S. L., 1995. Partial melting and phase relations in high-grade metapelites: an experimental petrogenetic grid in KFMASH system. *Contributions to Mineralogy and Petrology*, **120,** 270–291.

Cartwright, I. & Barnicoat, A. C., 1986. The generation of quartz-normative melts and corundum-bearing restites by crustal anatexis; petrogenetic modelling based on an example from the Lewisian of North-west Scotland. *Journal of Metamorphic Geology*, **4,** 79–99.

Droop, G. T. R., Clemens, J. D. & Dalrymple, D. J., 2003. Processes and conditions during contact anatexis, melt escape and restite formation: the Huntly Gabbro complex, NE Scotland. *Journal of Petrology*, **44,** 995–1029.

Duran, H., 1985. *El Paleozoico de Les Guilleries*, PhD thesis. Universitat Autònoma de Barcelona, 243 pp.

Grant, J. A., 1985. Phase equilibria in low-pressure partial melting of pelitic rocks. *American Journal of Science*, **285,** 409–435.

Guiraud, M., Powell, R. & Rebay, G., 2001. H_2O in metamorphism and unexpected behaviour in the preservation of metamorphic mineral assemblages. *Journal of Metamorphic Geology*, **19,** 445–454.

Holland, T. J. B. & Powell, R., 1998. An internally consistent thermodynamic dataset for phases of petrological interest. *Journal of Metamorphic Geology*, **16,** 309–343.

Holtz, F. & Johannes, W., 1996. *Petrogenesis and experimental petrology of Granitic Rocks*. Springer-Verlag, Berlin.

Johnson, T. E., Gibson, R. L., Brown, M., Buick, I. S. & Cartwright, I., 2003a. Partial melting of metapelitic rocks beneath the Bushveld Complex, South Africa. *Journal of Petrology*, **44,** 789–813.

Johnson, T. E., Brown, M. & Solar, G. S., 2003b. Low-pressure and suprasolidus phase equilibria in the MnNCKFMASH system: Constraints on conditions of regional metamorphism in western Maine, northern Appalachians. *American Mineralogist*, **88,** 624–638.

Kretz, R., 1983. Symbols for rock-forming minerals. *American Mineralogist*, **68,** 277–279.

Kriegsman, L. M., 2001. Partial melting, partial melt extraction and partial back reaction in anatectic migmatites. *Lithos*, **56,** 75–96.

McDade, P. & Harley, S.L., 2001. A petrogenetic grid for aluminous granulite facies metapelites in the KFMASH system. *Journal of Metamorphic Geology*, **19,** 45–59.

Mehnert, K. R., 1968. *Migmatites and the origin of granitic rocks*. Elsevier, New York.

Patiño Douce, A. E. & Johnston, A. D., 1991. Phase equilibria and melt productivity in the pelitic system: implications for the origin of peralominous granitoids and aluminous granulites. *Contributions to Mineralogy and Petrology*, **107,** 202–218.

Pattison, D. R. M. & Harte, B., 1991. Petrography and mineral chemistry of pelites. In: *Equilibrium and kinetics in contact metamorphism: The Ballachulish igneous complex and its aureole* (eds Voll, G., Topel, G., Pattison, D. R. M. & Seifert, F.) Springer-Verlag, Heidelberg.

Powell, R. & Downes, J., 1990. In: *Garnet porphyroblast–bearing leucosomes in metapelites: mechanisms, phase diagrams, and an example from Broken Hill, Australia. High-Temperature metamorphism and crustal anatexis* (eds Ashworth, J. R. & Brown, M.), pp. 105–123. Unwin, London.

Powell, R. & Holland, T. J. B., 1988. An internally consistent thermodynamic dataset with uncertainties and correlation. Application, methods, worked examples and a computer program. *Journal of Metamorphic Geology*, **6,** 173–204.

Reche, J. & Martinez, F. J., 2002. Evolution of bulk composition, mineralogy, strain style and fluid flow during an HT-LP metamorphic event: sillimanite zone in the Catalonian Coastal Ranges Variscan basement, NE Iberia. *Tectonophysics*, **348,** 111–134.

Sebastian, A., Reche, J. & Duran, H., 1990. Hercynian metamorphism in the Catalonian coastal ranges. *Acta geologica hispanica*, **255,** 31–32.

Spear, F. S., Kohn, M. J. & Cheney, J. T., 1999. P–T paths from anatectic pelites. *Contributions to Mineralogy and Petrology*, **134,** 17–32.

Stüwe, K., 1997. Effective bulk composition changes due to cooling: a model predicting complexities in retrograde reaction textures. *Contributions to Mineralogy and Petrology*, **129,** 43–52.

Stüwe, K. & Powell, R., 1989a. Metamorphic segregations associated with garnet and orthopyroxene porphyroblast growth: two examples from the Larsemann Hills, east Antarctica. *Contributions to Mineralogy and Petrology*, **103,** 523–530.

Stüwe, K. & Powell, R., 1989b. Metamorphic evolution of the Bunger Hills, East Antarctica; evidence for substantial post-metamorphic peak compression with minimal cooling in a Proterozoic orogenic event. *Journal of Metamorphic Geology*, **7,** 449–464.

White, R. W. & Powell, R., 2002. Melt loss and the preservation of granulite facies mineral assemblages. *Journal of Metamorphic Geology*, **20,** 621–632.

White, R. W., Powell, R. & Holland, T. J. B., 2001. Calculation of partial melting equilibria in the system Na_2O–CaO–K_2O–FeO–MgO–Al_2O_3–SiO_2–H_2O (NCKFMASH). *Journal of Metamorphic Geology*, **19,** 139–153.

White, R. W., Powell, R. & Clarke, G.L., 2003. Prograde metamorphic assemblage evolution during partial melting of metasedimentary rocks at low pressures: migmatites from Mt Stafford, Central Australia. *Journal of Petrology*, **44,** 1937–1960.

Received 16 July 2003; revision accepted 8 April 2004.

APPENDIX

MINERAL CHEMISTRY OF THE SUSQUEDA CONTACT AUREOLE AND ANALYTICAL METHODS

Major element concentration were analysed by X-ray fluorescence (XRF) spectrometry in the Serveis cientifico-tècnics of the Universitat de Barcelona. Microprobe analyses were carried out on the Cameca SX-50 electron microprobe housed at the Servicios cientifico-tècnics in the Universitat de Barcelona operating with the accelerating voltage of 15 kV, a beam current of 10 nA and an integration time of 10 s. Representative mineral compositions from a total of about 100 thin sections of different rock types from the aureole are given in Table 3.

Garnet in hornfels-I is almandine rich and compositionally similar in all the samples. They are characterised by $X_{Alm} = 0.84$–0.86 where $X_{Alm} = Fe/(Fe + Mg + Ca + Mn)$ and $X_{Py} = 0.13$–0.14 where $X_{Py} = Mg/(Fe + Mg + Ca + Mn)$. The Mn content $X_{Sps} = Mn/(Fe + Mg + Ca + Mn)$ is no higher than $X_{Sps} = 0.02$ and Ca contents are lower than $X_{Grs} = 0.04$, where $X_{Grs} = Ca/(Fe + Mg + Ca + Mn)$. All garnet has commonly a more or less broad retrograde rim where Mn component increase progressively up to $X_{Sps} = 0.07$, Fe increases to $X_{Alm} = 0.92$–0.94. and the Mg proportion decreases down to $X_{Py} = 0.14$. Garnets in restites are also homogeneous, but have higher magnesium ratios $X_{Py} = 0.21$–0.22. The relative Mn (X_{Sps} *c.* 0.02) and Ca (X_{Grs} *c.* 0.04) show no remarkable differences compared with hornfels-I. Garnets show commonly rims of elevated XFe, but these are narrower than in those garnets in the hornfels-I. The Mn increase up to $X_{Sps} = 0.04$ and the garnets are Fe richer X_{Alm} *c.* 0.84 and Mg poorer X_{Py} *c.* 0.09.

The composition of biotite is very similar in all rock types except for biotite in restites which are Fe poorer ($X_{Fe} = 0.57$–0.62) than biotite from the hornfelses ($X_{Fe} = 0.65$–0.69). The absence of remarkable differences can be a consequence of the high chemical diffusion in biotite which allows an homogenisation of biotite compositions after peak conditions. In sample MR-99-36 the relic biotite included in cordierite (Fig. 4d) show no differences with the matrix biotite analysed in the same sample.

Cordierite in the micaschists has a composition of $X_{Fe} = 0.47$. Cordierite in hornfels-I and -II have a similar $X_{Fe} = 0.46$–0.49, whereas cordierite in restites have higher Fe contents ($X_{Fe} = 0.51$). The Mn content is significant in hornfels-II with 0.05–0.06 mol.% Mn, while cordierite in garnet-bearing rocks shows very low Mn cation contents lower than 0.02. Cordierite in restites has lower iron contents ($X_{Fe} = 0.44$–0.46) than those in hornfelses. Cordierite inclusions in garnet have very low iron contents down to $X_{Fe} = 0.31$. These inclusions are believed to form at higher *P–T* conditions and are preserved as relic cordierite compositions protected by garnet from re-equilibration at lower temperatures.

Spinel occurs in two different compositional varieties: spinel wrapped by andalusite in hornfels-II, and spinel in restites. Spinel in hornfels-II is iron-rich values of hercynite ranging from He_{69} to He_{83}, ($He = Fe/(Fe + Mg + Zn + Mn)$. The Zn represented by the gahnite component: $Gh = Zn/(Fe + Mg + Zn + Mn)$ can range from Gh_{07} to Gh_{24} in different spinels from the same sample. The magnesium content is defined by the spinel end member, $Sp = Mg/(Fe + Mg + Zn + Mn)$ and has values from Sp_{09} to Sp_{11}. Spinel in restites has a similar composition range to the spinel in the silica-undersaturated rocks: $He_{70–75}$, $Gh_{16–19}$, $Sp_{09–11}$.

Plagioclase shows a remarkable compositional variation even within the same sample. For example, within sample Br3 $An = Ca/(Ca + Na)$ varies between An_{16} and An_{47} (Table 3). Plagioclases embedded in restites have also complex zonations and have high calcium contents (An_{61}–An_{70}). In contrast, plagioclase analysed in the trondhjemitic pockets of the hornfelses is homogeneous and sodium richer (An_{08}–An_{09}).

Table 3. Selected mineral analysis in different rock types (a) garnet, (b) cordierite; *mat.* = mineral in the matrix; *inc.* = present as inclusion, (c) plagioclase, (d) biotite and (e) spinels.

	Hornfels-I				Restites			
Wt% oxide	99-36	99-36	Br-3	Br-3	98-5*	98-5*	98-6	98-6
(a) Garnet								
SiO_2	36.53	35.81	37.07	36.80	37.58	36.66	38.03	38.16
TiO_2	0.04	0.08	0.15	0.14	0.16	0.14	0.08	0.07
Al_2O_3	21.05	20.91	21.04	20.34	20.94	20.46	21.48	20.75
Fe_2O_3	1.74	2.16	0.53	0.46	–	–	0.10	0.43
FeO	34.97	36.34	35.62	36.58	34.74	37.77	32.84	36.16
MnO	0.81	1.55	0.75	3.10	0.74	1.27	0.76	1.32
MgO	3.37	1.82	3.46	1.20	5.27	2.40	5.51	2.25
CaO	1.42	1.31	1.50	1.39	1.01	1.48	1.66	1.66
Na_2O	0.02	0.01	0.00	0.00	0.02	0.00	0.00	0.02
K_2O	0.00	0.00	0.00	0.00	0.01	0.03	0.00	0.00
Total	99.95	99.99	100.12	100.01	100.47	100.20	100.46	100.82
Cations on 8 Oxygen								
Si	2.95	2.92	2.98	3.01	2.98	2.98	2.99	3.05
Ti	0.00	0.01	0.01	0.01	0.01	0.01	0.01	0.00
Al	2.00	2.01	1.99	1.96	1.96	1.96	1.99	1.95
Fe^{3+}	0.11	0.13	0.03	0.03	–	–	0.01	0.03
Fe^{2+}	2.36	2.48	2.39	2.50	2.31	2.57	2.16	2.42
Mn	0.06	0.11	0.05	0.22	0.05	0.09	0.05	0.09
Mg	0.41	0.22	0.41	0.15	0.62	0.29	0.65	0.27
Ca	0.12	0.12	0.13	0.12	0.00	0.13	0.14	0.14
Na	0.00	0.00	0.00	0.00	0.09	0.01	0.00	0.00
K	0.00	0.00	0.00	0.00	0.00	0.00	0.00	0.00
Cations sum	8.00	8.00	8.00	7.99	8.02	8.03	7.99	7.95
X_{Fe}	0.85	0.92	0.85	0.94	0.79	0.90	0.77	0.90
X_{Alm}	0.80	0.85	0.80	0.84	0.77	0.84	0.72	0.83
X_{Sps}	0.02	0.04	0.02	0.07	0.02	0.03	0.02	0.03
X_{Py}	0.14	0.08	0.14	0.05	0.21	0.09	0.22	0.09
X_{Grs}	0.04	0.04	0.04	0.04	0.00	0.04	0.05	0.05

	Micaschist	Phornfels-I			Hornfels-II.		Restites		
Wt% oxide	99-14	99-30	99-36	99-36	99-22-1	99-22-2	98-24	98-5 inc.*	98-5 mat.*
(b) Cordierite									
SiO_2	46.43	47.38	47.65	47.69	47.2	47.23	47.1	48.17	48.00
TiO_2	0.04	0.00	0.00	0.04	0	0	0	0.00	0.00
Al_2O_3	32.48	32.74	32.45	32.72	31.76	31.46	32.3	32.66	32.25
Fe_2O_3	0.79	2.07	1.98	1.55	1.4	1.72	2.55	–	–
FeO	9.61	10.36	9.92	10.21	10.29	10.61	9.18	7.66	10.22
MnO	0.24	0.12	0.20	0.19	0.454	0.386	0.31	0.07	0.16
MgO	6.03	5.91	6.55	6.27	5.54	5.76	6.07	9.39	7.27
CaO	0.00	0.03	0.01	0.00	0.01	0.03	0.01	0.05	0.03
Na_2O	0.28	0.25	0.14	0.21	0.43	0.23	0.38	0.13	0.08
K_2O	0.00	0.00	0.00	0.00	0.04	0	0.02	0.00	0.02
Total	95.90	98.86	98.90	98.88	97.12	97.43	97.92	98.12	98.02
Cations on 11 Oxygen									
Si	4.95	4.94	4.95	4.93	4.92	4.93	4.94	4.96	5.00
Ti	0.00	0.00	0.00	0.00	0.00	0.00	0.00	0.00	0.00
Al	4.09	4.02	3.97	4.00	3.98	3.94	4.00	3.96	3.96
Fe^{3+}	0.06	0.18	0.16	0.12	0.10	0.14	0.20	–	–
Fe^{2+}	0.86	0.88	0.86	0.89	0.92	0.95	0.81	0.66	0.89
Mn	0.02	0.01	0.02	0.01	0.06	0.05	0.03	0.01	0.01
Mg	0.96	0.92	1.01	0.95	0.88	0.92	0.95	1.44	1.13
Ca	0.00	0.00	0.00	0.00	0.00	0.00	0.00	0.01	0.00
Na	0.06	0.05	0.03	0.04	0.08	0.05	0.08	0.03	0.02
K	0.00	0.00	0.00	0.00	0.01	0.00	0.00	0.00	0.00
Cations sum	11.00	11.00	11.00	10.94	10.95	10.98	11.00	11.06	11.02
X_{Fe}	0.47	0.49	0.46	0.48	0.51	0.51	0.46	0.31	0.44

Rock type	Hornfels-I				Hornfels-II		Restites		
Sample	99-30	99-30	Br-3	Br-3	99-22-1	99-22-2	98-5	98-5	98-5
(c) Plagioclase									
SiO_2	55.94	56.16	64.17	56.36	66.17	66.34	50.44	52.27	52.98
TiO_2	0.01	0.00	0.00	0.00	0.02	0.02	0.01	0.00	0.03
Al_2O_3	25.95	27.33	21.71	26.34	20.52	20.67	31.34	29.97	29.61
FeO	0.12	0.08	0.14	0.00	0.12	0.05	0.00	0.04	0.05
MnO	0.00	0.02	0.00	0.01	0.02	0.00	0.08	0.00	0.03

Table 3. (*Cont'd*).

Rock type	Hornfels-I				Hornfels-II		Restites		
Sample	99-30	99-30	Br-3	Br-3	99-22-1	99-22-2	98-5	98-5	98-5
MgO	0.02	0.01	0.00	0.00	0.03	0.00	0.06	0.15	0.02
CaO	9.12	9.91	3.41	9.43	1.74	1.78	14.25	12.86	12.47
Na_2O	6.57	6.23	9.71	6.27	10.27	10.91	3.33	4.07	4.39
K_2O	0.12	0.10	0.08	0.08	0.11	0.08	0.02	0.02	0.04
Total	97.84	99.76	99.23	98.49	98.99	99.84	99.54	99.40	99.61
Cations on 8 Oxygen									
Si	2.64	2.53	2.85	2.57	2.93	2.92	2.31	2.38	2.41
Ti	0.00	0.00	0.00	0.00	0.00	0.00	0.00	0.00	0.00
Al	1.35	1.45	1.14	1.41	1.07	1.07	1.69	1.61	1.59
Fe^{2+}	0.00	0.00	0.01	0.00	0.00	0.00	0.00	0.00	0.00
Mn	0.00	0.00	0.00	0.00	0.00	0.00	0.00	0.00	0.00
Mg	0.00	0.00	0.00	0.00	0.00	0.00	0.00	0.01	0.00
Ca	0.37	0.48	0.16	0.46	0.08	0.08	0.70	0.63	0.61
Na	0.64	0.54	0.84	0.55	0.88	0.93	0.30	0.36	0.39
K	0.01	0.01	0.00	0.00	0.01	0.00	0.00	0.00	0.00
Total	5.01	5.02	5.00	5.00	4.98	5.01	4.99	4.99	5.01
X_{An}	0.37	0.47	0.16	0.45	0.09	0.08	0.70	0.63	0.61

	Micashists		Hornfels-I			Hornfels-II			Restite		
Sample	99-14	99-14	99-24	99-30	99-36	99-25-2	99-22-1		98-24	98-5*	98-6
(d) Biotite											
SiO_2	34.04	34.34	34.04	34.63	35.25	33.24	33.99	34.13	34.4	34.06	33.34
TiO_2	2.19	3.11	2.75	2.06	2.31	2.01	2.36	2.19	2.91	2.27	1.52
Al_2O_3	20.69	19.85	20.51	19.92	20.07	20.72	19.54	20.02	19.8	19.79	21.06
FeO	21.52	21.05	23.37	24.23	23.49	24.1	23.02	22.64	22.3	21.98	21.34
MnO	0.09	0.11	0.01	0.12	0.00	0.15	0.14	0.14	0.02	0.01	0.06
MgO	6.49	6.38	6.62	6.46	5.85	6.22	6.93	6.57	7.54	8.58	8.93
CaO	0.00	0.01	0.00	0.06	0.04	0.07	0.00	0.00	0.00	0.04	0.05
Na_2O	0.21	0.16	0.26	0.18	0.2	0.18	0.18	0.18	0.31	0.13	0.11
K_2O	8.53	8.34	8.74	8.52	8.17	7.44	8.86	9.1	8.63	7.32	6.32
Total	93.76	93.35	96.30	96.18	95.38	94.13	95.02	94.97	95.9	94.22	93.00
Cations on 11 Oxygen											
Si	2.65	2.68	2.61	2.66	2.71	2.58	2.64	2.65	2.65	2.63	2.58
Ti	0.13	0.18	0.16	0.12	0.13	0.12	0.14	0.13	0.17	0.13	0.09
Al	1.9	1.82	1.85	1.8	1.82	1.9	1.79	1.83	1.8	1.8	1.92
Fe^{2+}	1.4	1.37	1.5	1.56	1.51	1.57	1.5	1.47	1.4	1.42	1.38
Mn	0.01	0.01	0.00	0.01	0.00	0.01	0.01	0.01	0.00	0.00	0.00
Mg	0.75	0.74	0.76	0.74	0.67	0.72	0.8	0.76	0.85	0.99	1.03
Ca	0.00	0.00	0.00	0.01	0.00	0.01	0.00	0.00	0.00	0.00	0.01
Na	0.03	0.02	0.04	0.03	0.03	0.03	0.03	0.03	0.05	0.02	0.02
K	0.85	0.83	0.85	0.84	0.80	0.74	0.88	0.9	0.85	0.72	0.62
Total	7.71	7.66	7.76	7.75	7.67	7.66	7.78	7.77	7.76	7.71	7.68
X_{Fe}	0.65	0.65	0.66	0.68	0.69	0.68	0.65	0.66	0.62	0.59	0.57
Al_{IV}	1.22	1.14	1.24	1.22	1.16	1.30	1.22	1.22	1.19	1.24	1.33
Al_{VI}	0.68	0.68	0.61	0.58	0.66	0.60	0.57	0.61	0.61	0.56	0.59

	Hornfels-II				Restite
Sample	99-22-1		99-25-2		98-6
(e) Spinel					
SiO_2	0.04	0.09	0.05	0.03	0.08	0.04
TiO_2	0.04	0.03	0.03	0.01	0.06	0.04
Al_2O_3	57.58	57.80	57.80	58.26	56.05	57.66
Cr_2O_3	0.07	0.04	0.05	0.05	1.11	0.04
FeO	33.81	33.86	34.88	34.78	29.12	31.39
MnO	0.24	0.32	0.27	0.39	0.09	0.16
MgO	2.31	2.32	2.49	2.54	2.45	2.16
ZnO	4.47	4.54	3.26	3.30	9.03	7.33
Total	98.56	98.99	98.84	99.36	98.03	98.84
Cations on 4 Oxygen						
Si	0.00	0.00	0.00	0.00	0.00	0.00
Al	1.98	1.98	1.98	1.98	1.95	1.98
Ti	0.00	0.00	0.00	0.00	0.00	0.00
Cr	0.00	0.00	0.00	0.00	0.03	0.00
Mg	0.10	0.10	0.11	0.11	0.11	0.09
Fe^{2+}	0.82	0.82	0.85	0.84	0.72	0.77

Table 3. (*Cont'd*).

	Hornfels-II				Restite	
Sample	99-22-1		99-25-2		98-6	
Mn	0.01	0.01	0.01	0.01	0.00	0.00
Zn	0.10	0.10	0.07	0.07	0.20	0.16
Total	3.01	3.01	3.01	3.01	3.01	3.01
Gh	0.09	0.10	0.07	0.07	0.19	0.16
Hc	0.81	0.81	0.83	0.82	0.70	0.75
Sp	0.10	0.10	0.11	0.11	0.11	0.09

Fe_2O_3 estimates are done after microprobe software corrections.
*All Fe analysed as FeO.